ACS OMEGA

http://pubs.acs.org/journal/acsodf

Article

Defect Passivation via Isoxazole Doping in Perovskite Solar Cells

Jinho Yoon, Xuewen Liu, and Eun-Cheol Lee*

Cite This: *ACS Omega* 2022, 7, 34278−34285

Read Online

ACCESS | Metrics & More | Article Recommendations | Supporting Information

ABSTRACT: To improve perovskite solar cell (PSC) performance, which is deeply related to perovskite layer quality, researchers have explored numerous strategies. Additive doping into perovskite precursors has been widely used to improve the PSC performance. In this study, we used isoxazole—a Lewis-base small molecule—as an additive for the $CH_3NH_3PbI_3$ ($MAPbI_3$) precursor and explored how isoxazole effectively passivates defects in the perovskite structure. We found that isoxazole interacted with undercoordinated Pb^{2+} ions from an X-ray photoelectron spectroscopy survey and verified that isoxazole doping improved the device performance. When the optimized concentration of isoxazole was doped in the $MAPbI_3$ precursor, the power conversion efficiency increased from 15.6 to 17.5%, with an improved fill factor and short-circuit current density. In addition, an isoxazole-doped device sustained 94% of its initial performance after 8 days under ambient air conditions (10 ± 5 RH %, 25 °C), whereas a device without isoxazole doping only maintained 64% of its initial performance.

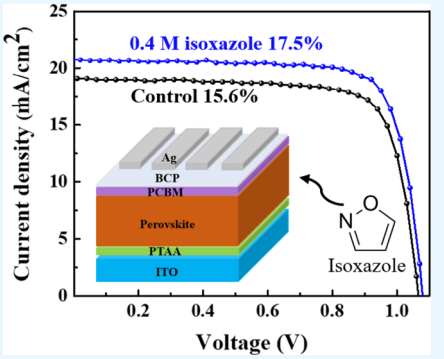

1. INTRODUCTION

To solve the fuel energy problems, solar energy has been considered an alternative future energy source.[1] Perovskite solar cells (PSCs) have been widely researched for solar energy generation applications due to advantages such as cost-effective fabrication,[2] easy fabrication processes,[3] tunable band gaps,[4] long carrier lifetimes,[5] and high absorption coefficients.[6] In particular, the inorganic−organic hybrid PSCs based on $CH_3NH_3PbI_3$ ($MAPbI_3$) have been studied extensively.[7−16] The power conversion efficiency (PCE) of PSCs has increased tremendously from 3.9 to 25.7% over the past 11 years.[17,18] Furthermore, an inverted PSC with the p−i−n structure has attracted considerable attention due to its metal oxide-free layer and low processing temperature.[19]

Meanwhile, defects in perovskites are responsible for nonradiative recombination,[20] and thus, their passivation has attracted much attention for use in suppressing defect-induced PSC degradation. Many researchers have explored defect passivation through molecular interactions between defects and various functional groups.[15,21−26] Particularly, Lewis-base molecules contain N,[27−29] S,[27,28,30−32] O,[33−35] and P[36,37] and hence can donate nonbonding electrons, reacting with and passivating undercoordinated Pb^{2+} ions or Pb clusters, which act as a nonradiative recombination center and induce perovskite phase degradation by reacting with O_2 and H_2O.[38] Compared with large Lewis-base molecules, small Lewis-base molecules might easily diffuse into the interior of bulk perovskites and hence are efficient for bulk defect passivation, whereas they can easily escape from the crystal, unable to passivate defects. Therefore, it is crucial to discover small molecules that improve the performance of PSCs. Previous studies have reported that poly(1-vinyl-3-ethyl-acetate) imidazole tetrafluoroborate,[39] bithiophene-based n-type conjugated small molecules,[40] 4-dimethylaminopyridine,[41] and dicyandiamide[42] can serve as small-molecule additives for PSCs to improve their performance.

In this study, we used isoxazole—a small Lewis-base molecule—as an additive to the perovskite precursor for improving the PSC performance. Isoxazole is a weak base heterocyclic compound containing both N and O atoms,[43] whose molecular structure is shown in Figure S1, and it has been widely used in drug synthesis.[44,45] We explored how this compound played a role in the perovskite structure and demonstrated that a small amount of isoxazole doping enhanced the PSC performance and reduced nonradiative recombination by the defect passivation. Doping 0.4 M isoxazole into the perovskite precursor improved the PCE of the best device from 15.63 to 17.50% with a great increase in J_{SC}. In addition, the isoxazole-added device retained 94% of its initial PCE under ambient air conditions (10 ± 5 RH %, 25 °C) after 8 day storage, indicating that it had better stability than the control device without isoxazole doping, which retained only 64% of its initial PCE.

Received: June 17, 2022
Accepted: September 1, 2022
Published: September 12, 2022

2. EXPERIMENTAL SECTION

2.1. Materials. Greatcell Solar Materials Pty Ltd. (Queanbeyan, Australia) produced methylammonium iodide (MAI). Bathocuproine (BCP) and lead(II) iodide (PbI_2) were obtained from TCI (Tokyo, Japan). Indium tin oxide (ITO)-patterned glass was obtained from Zhuhai Kaivo Optoelectronic Technology Co., Ltd. (Zhuhai, China). Sigma-Aldrich (St. Louis, MO, United States) provided chlorobenzene (CB), isoxazole, *N*,*N*-dimethylformamide (DMF), poly[bis(4-phenyl)(2,4,6-trimethylphenyl)amine] (PTAA), dimethyl sulfoxide (DMSO), Hellmanex III for detergent, and isopropyl alcohol (IPA). Nano-C Inc. (Westwood, MA, United States) provided [6,6]-phenyl-C_{61}-butyric acid methyl ester (PCBM). All these chemical materials were used without any purification.

2.2. Device Fabrication. About 1.2 M PbI_2 (553 mg) and 1.2 M MAI (190 mg) were added to DMF (700 μL) and DMSO (300 μL) for the precursor preparation. We added 0.2, 0.4, or 0.6 M isoxazole into the precursor solution for the experimental sample preparation, whereas no isoxazole was added for the control sample. All precursors were stored for 12 h at room temperature. For the hole-transport layer, 1.5 mg of PTAA was dissolved in 1 mL of toluene. For the electron transport layer, PCBM (20 mg/mL in CB) and BCP (1.5 mg/mL in IPA) were heated for 2 h on a hot plate at 60 °C. For device fabrication, ITO-coated glass was cleansed by ultrasonic treatment sequentially with a detergent, deionized water, and IPA for 25 min each. After cleaning, the substrates were treated with ultraviolet (UV) ozone plasma for 30 min. We coated the PTAA layer on a substrate via a spin-coating process at 4000 rpm for 33 s (initial 3 s for acceleration), followed by a heating procedure at 120 °C for 10 min. The perovskite layer was deposited on the PTAA-coated substrate at 1000 rpm for 10 s and 5000 rpm for 35 s, for which acceleration times were 1 and 5 s, respectively. 15 s after the second acceleration, CB (350 μL) was dripped on the substrate. After depositing the active layer, we put the sample on a hot plate at 60 °C for 30 s and 90 °C for 20 min. The next step was spin-coating PCBM (60 μL) and BCP (60 μL) at 1500 rpm for 30 s and 4000 rpm for 30 s, respectively, with an acceleration time of 5 s. From the PTAA deposition to BCP fabrication, all steps were performed in a glove box filled with nitrogen gas. As the last step, Ag (100 nm) deposition on the electrode was conducted using a thermal evaporator under high-vacuum conditions (<8.0 × 10^{-6} Torr).

2.3. Characterization. We employed scanning electron microscopy (SEM) to observe the surface morphologies using JSM-7500F (JEOL, Tokyo, Japan). We used SmartLab (Rigaku, Tokyo, Japan) to study the X-ray diffraction (XRD) pattern of our $MAPbI_3$-coated films. The Fourier transform infrared (FTIR) spectra were recorded using a Spectrum Two instrument (PerkinElmer, MA, United states) with a resolution of 2 cm^{-1}. The current density−voltage (J−V) curve results and space-charge-limited current (SCLC) measurement were obtained using a Keithley 2400 source meter (Keithley, Cleveland, OH, United States) under illuminated and dark conditions. The standard 1 sun illumination condition (AM 1.5 G, 100 mW/cm^2) was controlled using HAL-320 (Asahi spectra USA, Torrance, CA, United States). To probe the incident photon-to-current efficiency (IPCE), we employed Solar Cell Scan 100 (Zolix Instruments, Beijing, China). For X-ray photoelectron spectroscopy (XPS), we used AXIS-Nova (Kratos Inc., San Diego, CA, United States) to assess the binding energy of each perovskite film surface molecule. Time-resolved photoluminescence (TRPL) and photoluminescence (PL) measurements were obtained using Fluorolog3 (HORIBA, Kyoto, Japan); the excitation wavelength for PL and TRPL was 467 nm and the emission wavelength for TRPL was 750 nm. UV−visible (UV−vis) spectroscopy analysis was obtained using Ultra-3660 (Rigol, Beijing, China). Electrochemical impedance spectroscopy (EIS) was performed using VersaSTAT3 (Ametek Scientific Instruments, Berwyn, PA, United States) under dark-room conditions. All these characterizations and analyses were obtained under ambient air conditions without the capsulation process. To estimate the average grain size, we calculate the average area of the grain by dividing the entire SEM image area by the total number of grains, assuming that the grain shape is a perfect circle (in two dimensions), and regard the diameter as the lateral size.

3. RESULTS AND DISCUSSION

Figure 1a−d shows top-view SEM images of perovskite films with different isoxazole concentrations. SEM results show that

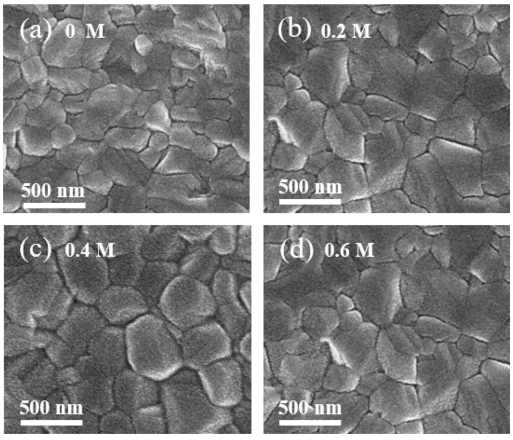

Figure 1. (a−d) Top-view SEM images of the $MAPbI_3$ perovskite film while increasing the isoxazole-doping concentration from 0 to 0.6 M.

the control film and 0.2−0.6 M isoxazole-doped films showed similar film compactness. Notably, isoxazole-doped films had larger average grain sizes than the control film of 241 nm; that is, 310, 342, and 319 nm for 0.2, 0.4, and 0.6 M isoxazole-doping concentrations, respectively. Films filled with a larger grain have fewer grain boundaries, which may decrease the nonradiative recombination of carriers.[46]

To explore the effect of isoxazole doping on the formation and crystallinity of perovskite phases, we measured the XRD patterns for perovskite films fabricated on ITO-patterned substrates. Figure 2a shows that all XRD patterns have two characteristic peaks of the perovskite structure at 14.10 and 28.42°, which are consistent with the (110) and (220) lattice planes, respectively.[47] Besides, the isoxazole-coated films do not have any new characteristic peaks compared with the control film, indicating that the additive did not induce a new phase. The 0.4 M isoxazole-doped perovskite film has the highest peak intensity value at those peaks, indicating that it has the best crystallinity. As shown in Figure S1, isoxazole—the Lewis base—has N and O atoms and hence can react with and passivate the undercoordinated Pb clusters or Pb^{2+} ions on the surface, which behave as charge traps,[48] by providing lone

https://doi.org/10.1021/acsomega.2c03775
ACS Omega 2022, 7, 34278−34285

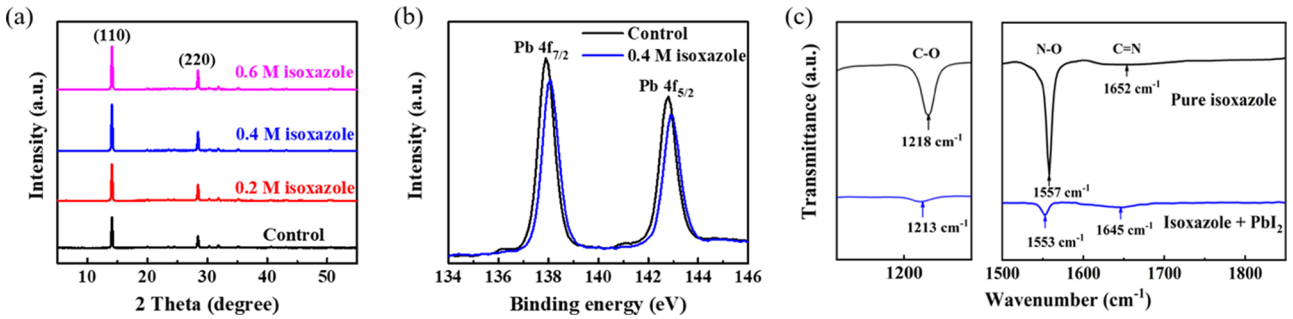

Figure 2. (a) XRD patterns and (b) XPS data for Pb $4f_{7/2}$ and Pb $4f_{5/2}$ spectra of control and 0.4 M isoxazole-doped films. (c) FTIR spectra of isoxazole with and without PbI_2.

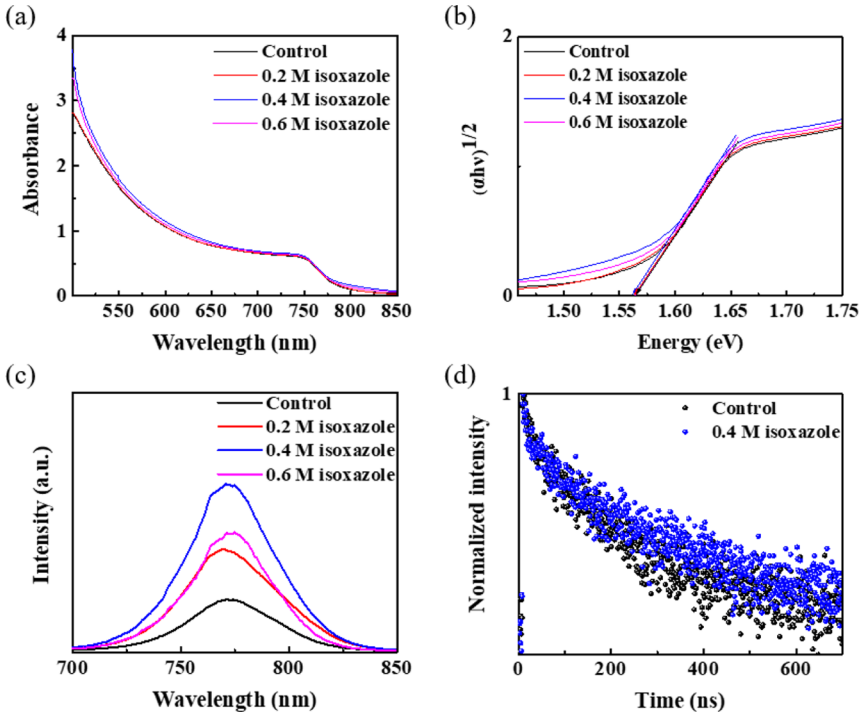

Figure 3. (a) UV−vis absorption spectra, (b) Tauc plots, and (c) PL spectra of perovskite films with increasing doping concentration. (d) TRPL spectra of the control and 0.4 M isoxazole-doped films.

pair electrons. We performed XPS measurements to examine the perovskite film surface with and without isoxazole doping (Figure 2b). High-resolution XPS results of Pb 4f for the control film displayed two specific peaks at 137.90 and 142.78 eV, corresponding to Pb $4f_{7/2}$ and Pb $4f_{5/2}$,[49,50] whereas the isoxazole-doped film had two peaks at 138.09 and 142.95 eV, respectively. Both peaks shift to higher binding energies by 0.19−0.17 eV, indicating that isoxazole anchored and reacted with Pb ions on the perovskite surface.[51] In the 0.4 M isoxazole-doped sample, the intensities of characteristic peaks were lower than those in the control sample. This may be due to the fact that isoxazole molecules on the surface block some of the incident X-rays. However, as discussed above, XRD data indicated that the crystallinity of the perovskite film was best for the case with 0.4 M isoxazole, although some isoxazole molecules might be located at the film surface.

To further verify the interaction between isoxazole and Pb^{2+} ions, we carried out FTIR spectroscopy measurements for 100.0 μL of isoxazole with and without 0.5 mg of PbI_2. As shown in Figure 2c, the stretching vibrations of C═N, N−O, and C−O bonds were 1652, 1557, and 1218 cm^{-1} in pure isoxazole[23,52,53] and were red-shifted to 1645, 1553, and 1213 cm^{-1} upon adding PbI_2, respectively. The weakening of C═N, N−O, and C−O bonds might be due to the formation of coordinate bonds between N or O atoms in isoxazole and Pb^{2+} ions in PbI_2, implying the attractive interaction between isoxazole and $MAPbI_3$, similar to previous studies.[54]

To further investigate the isoxazole-doping effect, we measured the UV−vis absorption spectra of the control and isoxazole-doped perovskite films deposited on glass substrates (Figure 3a). Figure 3a shows that all films have almost the same absorption edge at ca. 770 nm, and the Tauc plot in Figure 3b shows that the band gaps of films are almost the same, that is, 1.56 eV, which is similar to the theoretically calculated band gap of the $MAPbI_3$ perovskite (1.5−1.6 eV).[55] This indicates that isoxazole doping slightly affects the band gap, which agrees with the SEM and XRD results, where no noticeable changes upon isoxazole doping were observed in the structure and morphology. The light absorption (Figure 3a,b) and steady-state PL (Figure 3c) for 0.4 M isoxazole doping were the highest among the considered films, indicating that optimized isoxazole doping can reduce defects and improve the

https://doi.org/10.1021/acsomega.2c03775
ACS Omega 2022, 7, 34278−34285

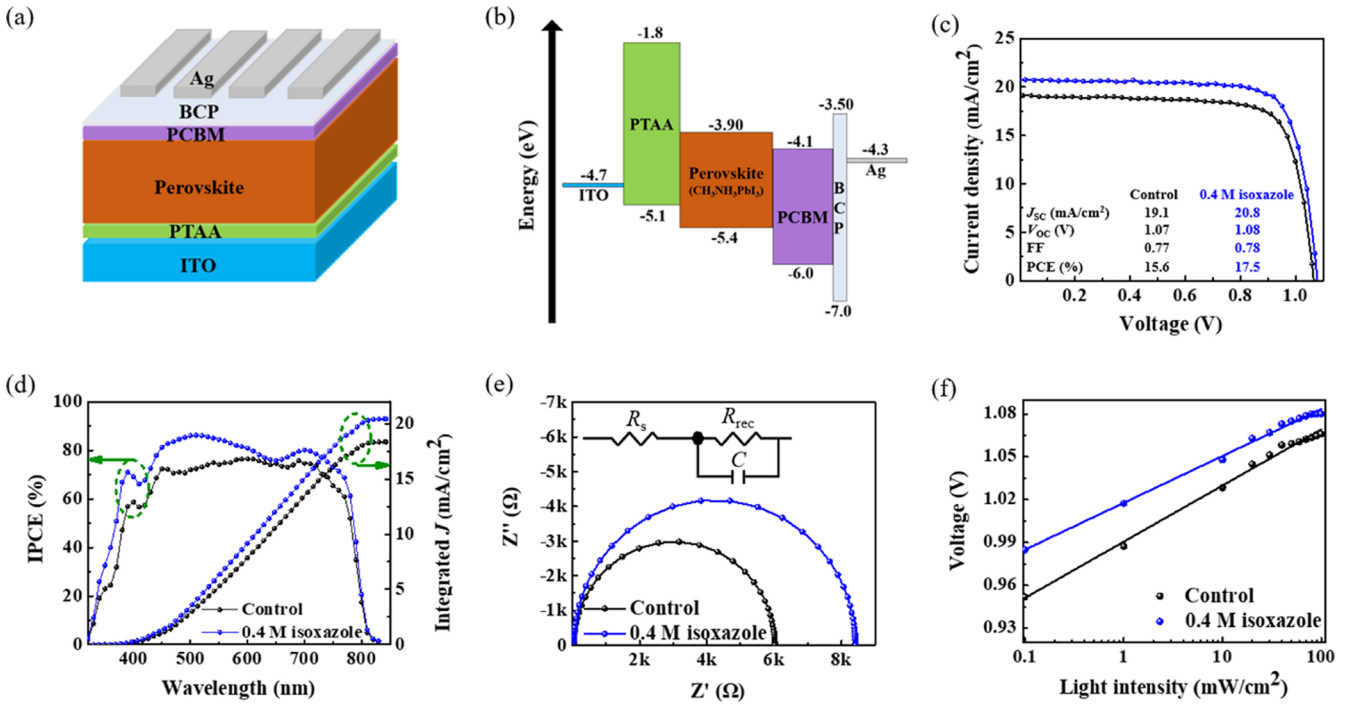

Figure 4. (a) Schematic structure and (b) energy band alignments of PSCs. (c) $J-V$ reverse scan curves, (d) IPCE and the integrated current density (integrated J) from the IPCE measurement using the AM 1.5 G photon flux spectrum, (e) EIS measurements, and (f) V_{OC} dependence on the light intensity of the control and 0.4 M isoxazole-doped devices.

crystallinity of the perovskite[56,57] and hence may enhance the PSC performance. To further explore the isoxazole-doping effect on charge carrier recombination dynamics, we performed the TRPL measurement (Figure 3d). The TRPL spectrum value can be obtained from a second-order exponential decay formula: $A_1e^{-t/\tau_1} + A_2e^{-t/\tau_2}$, where A_1 and A_2 denote the decay amplitudes and τ_1 and τ_2 denote the fast and slow decay times, respectively.[58] The 0.4 M isoxazole-doped film had a longer average PL decay time of 333.9 ns than the control film (282.3 ns) (Table S1), indicating that isoxazole doping can reduce the defects associated with nonradiative recombination.

We fabricated PSCs (Figure 4a) with a configuration of glass/ITO/PTAA/perovskite with or without isoxazole/PCBM/BCP/Ag with a 0.04 cm^2 active area to explore their photovoltaic performance. Figure S2 shows the cross-sectional SEM images of the device without isoxazole doping (the control device) and the 0.4 M isoxazole-doped device. The perovskite layer thicknesses of both devices are approximately 520 nm. Figure 4b shows that the energy band of each layer is well aligned for electron and hole transports, where the values of energy bands were obtained from previous studies.[59,60] Figure 4c shows the $J-V$ characteristic curve of the best device for each experimental group; the 0.4 M isoxazole-doped device showed a photovoltaic performance with a PCE of 17.5%, whereas the control device achieved such with a PCE of 15.6%. The $J-V$ curves of all different concentrations are shown in Figure S3, and the details of the photovoltaic parameters are shown in Table S2. The 0.4 M isoxazole-doped device had a 1.4 mA/cm^2 higher average short-circuit current (J_{SC}) than the control device, attributable to the suppression of electrically active defects responsible for nonradiative recombination through the reaction between isoxazole and Pb ions.[61] Figure S4 and Table S3 show the hysteresis results of each device and the detailed data under reverse scan (from V_{oc} to 0 V) and forward scan (from 0 V to V_{oc}). The hysteresis index (HI), which is given by $\frac{PCE_{reverse} - PCE_{forward}}{PCE_{reverse}}$,[62] reduced from 0.04 to 0.02 using an isoxazole additive, where $PCE_{reverse}$ and $PCE_{forward}$ indicate the power conversion efficiencies measured under reverse and forward bias conditions, respectively. This is also explained by defect passivation by isoxazole.[63,64] As shown in Figure S5 and Table S2, after adding isoxazole, the standard deviation of PCE decreased, implying that using isoxazole is beneficial for obtaining better device uniformity in mass production. The 0.4 M isoxazole-doped device showed the highest average PCE of (17.1%), which was 1.9% higher than that (15.2%) of the control device. The increases in J_{SC} and fill factor (FF) are mainly responsible for the PCE improvement, whereas the change in V_{OC} is negligible upon isoxazole doping. The average PCE for 0.6 M isoxazole doping was 16.3%, which decreased by 0.8% compared with that for the 0.4 M doping group. This is consistent with smaller perovskite grain sizes and worse crystallinity for 0.6 M isoxazole doping than those for 0.4 M isoxazole doping (Figures 1 and 2a). As seen from Figure 4d, the 0.4 M isoxazole-doped device shows a higher IPCE than the control device at wavelengths between 350 and 800 nm. The J_{SC} values obtained by integration of IPCE are 20.5 and 18.4 mA/cm^2 for the 0.4 M isoxazole-doped and control devices, respectively. These values are similar to the measured J_{SC} in Figure 4c, within 1.4%, indicating the high reliability of our results. EIS was performed under dark conditions to explore the carrier transfer process. Figure 4e shows the corresponding Nyquist plot and equivalent circuit that includes R_s and R_{rec}; R_s comprises the electrode and contact resistances between each layer,[65] and R_{rec} is the charge recombination resistance.[66] Figure 4e and Table S4 show that the R_{rec} value (8369 Ω) of the 0.4 M isoxazole-doped device is significantly larger than that of the control device (5966 Ω), showing suppressed charge recombination upon isoxazole

https://doi.org/10.1021/acsomega.2c03775
ACS Omega 2022, 7, 34278−34285

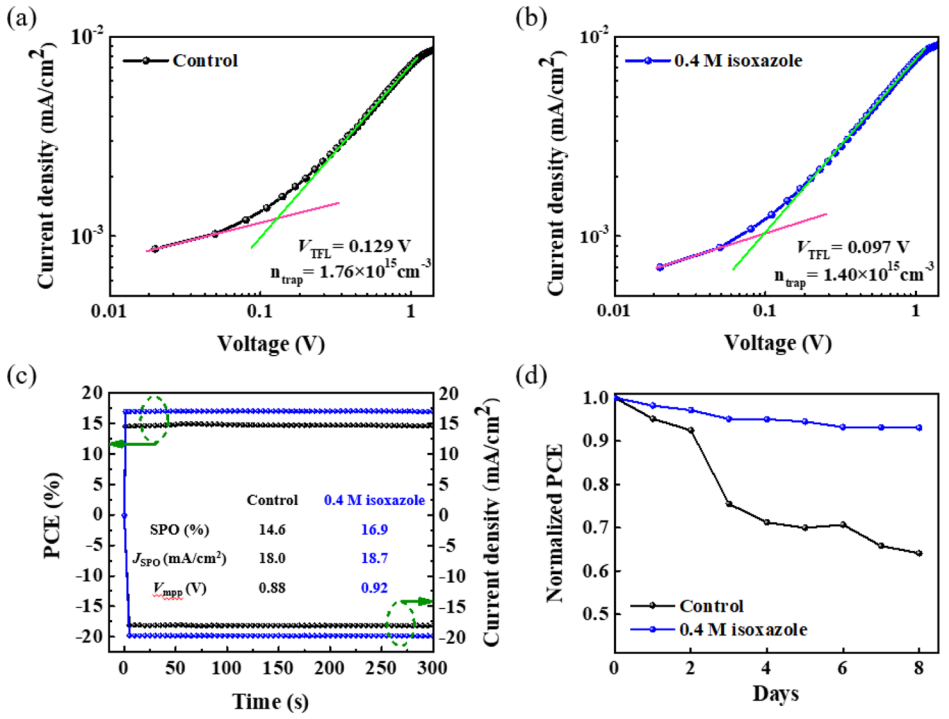

Figure 5. Dark J−V curves of the (a) control device and (b) 0.4 M isoxazole-doped device; (c) stabilized photocurrent densities and power output; and (d) stability measurement of the devices with and without isoxazole doping.

doping. To further probe into the charge recombination in the devices, we measured the light intensity dependence of V_{OC} for each device. The V_{OC} dependence on the light intensity (I) is given by $V_{OC} = nkT\ln(I)/e$ + constant, where T, e, k, and n are the absolute temperature, electron charge, Boltzmann constant, and ideality factor, respectively.[67,68] From the Shockley−Read−Hall recombination kinetics, a steeper slope ($n > 1$) denotes a higher trap state density of a device.[69] Figure 4f shows that the 0.4 M isoxazole-doped device has a lower slope (1.27 kT/e) than the control device (1.52 kT/e). The improved R_{rec} and the reduced n indicate that isoxazole doping can passivate charge traps in PSCs.

We obtained the SCLC to measure the trap density (n_{trap}) of each device comprising ITO/perovskites with and without the isoxazole/Ag structure under dark conditions. Figure 5a,b shows a linear Ohmic-type response at low bias voltages; if this voltage is greater than the kink point known as the trap-filled limit voltage (V_{TFL}), J_{SC} starts to show a significantly higher slope increase with voltage. V_{TFL} is given by $V_{TFL} = \frac{e}{2\varepsilon\varepsilon_0} n_{trap} L^2$,[70] where ε, ε_0, e, n_{trap}, and L denote the relative dielectric constant, vacuum permittivity, elementary charge, trap density, and thickness of the perovskite, respectively; ε = 32.[71] The thickness of the perovskite film was 520 nm, as discussed above. The calculated value of the trap density of the 0.4 M isoxazole-doped device was 1.40 × 10^{15} cm^{-3}—lower than that of the control device (1.76 × 10^{15} cm^{-3}). This agrees with the results of crystallinity, EIS, and light-intensity-dependent V_{OC} measurements and indicates that the isoxazole additive passivates defect-induced charge traps. Figure 5c shows the stabilized power output (SPO) and photocurrent density (J_{SPO}) at the maximum power point voltage (V_{mpp}). The 0.4 M isoxazole-doped device showed a more stable SPO of 16.9% and a J_{SPO} of 19.7 mA/cm^2 than those of the control device (14.6% and 18.0 mA/cm^2, respectively). We stored the devices without capsulation in ambient air to investigate PCE stability. As shown in Figure 5d, the normalized PCE of the 0.4 M isoxazole-doped device remained over 94% of the initial PCE after 8 days, whereas the control device retained only 64% of its initial PCE. It demonstrates that the isoxazole doping passivated the defects such as unsaturated Pb ions, which have coordinate bonds with O_2 and H_2O and hence cause perovskite film degradation.[38,72,73] The 0.4 M isoxazole-doped cell also showed the enhanced light soaking stability under illumination (see Figure S6), which was measured by a method similar to that in previous studies.[74,75] Our results indicate that isoxazole is an effective small-molecule additive for improving the efficiency and stability of inverted PSCs based on $MAPbI_3$. Further study is required to prove that isoxazole additives also improve the performances of different kinds of PSCs.

4. CONCLUSIONS

In summary, we improved the PCE of the optimal PSC from 15.6 to 17.5% via a small Lewis-base molecule isoxazole-doping technique. We found that isoxazole reacted with under-coordinated Pb^{2+} ion defects via XPS measurements, which agrees well with the reduction of electrically active charge traps by an isoxazole additive observed by TRPL, EIS, V_{OC} versus light intensity, and SCLC measurements. Furthermore, the isoxazole additive increased the PSC stability under ambient air conditions. Our results indicate that isoxazole is one of the promising small-molecule additives that may effectively passivate defects inside and near interfaces.

■ ASSOCIATED CONTENT

Supporting Information

The Supporting Information is available free of charge at https://pubs.acs.org/doi/10.1021/acsomega.2c03775.

https://doi.org/10.1021/acsomega.2c03775
ACS Omega 2022, 7, 34278−34285

Chemical structure of isoxazole; cross-sectional SEM image of the control and 0.4 M isoxazole-doped devices; $J-V$ reverse scan curves for the control and isoxazole-doped devices; $J-V$ forward scan curves for control and 0.4 M isoxazole-doped devices; statistics data of 15 devices with different isoxazole-doping concentrations; light soaking stability measurement under AM 1.5G illumination without encapsulation in air; detailed TRPL data of the control and 0.4 M isoxazole-doped films; device performance data for control and isoxazole-doped devices; and data of $J-V$ curves of reverse and forward scan and HI; and detailed EIS data of perovskite devices with and without isoxazole (PDF)

AUTHOR INFORMATION

Corresponding Author

Eun-Cheol Lee − *Department of Nanoscience and Technology, Graduate School and Department of Physics, Gachon University, Seongnam, Gyeonggi 13120, Republic of Korea;* orcid.org/0000-0002-8493-0031; Email: eclee@gachon.ac.kr

Authors

Jinho Yoon − *Department of Nanoscience and Technology, Graduate School, Gachon University, Seongnam, Gyeonggi 13120, Republic of Korea*

Xuewen Liu − *Department of Physics, Gachon University, Seongnam, Gyeonggi 13120, Republic of Korea;* orcid.org/0000-0002-8649-6080

Complete contact information is available at: https://pubs.acs.org/10.1021/acsomega.2c03775

Notes

The authors declare no competing financial interest.

ACKNOWLEDGMENTS

This work was supported by the National Research Foundation of Korea (NRF) grant funded by the Korea government (MSIT) (no. 2021R1F1A1051089) and the Gachon University Research Fund of 2020 (GCU-202008480006). The authors would like to thank Enago for the English language review.

REFERENCES

(1) Kannan, N.; Vakeesan, D. Solar energy for future world: - A review. *Renewable Sustainable Energy Rev.* **2016**, *62*, 1092−1105.

(2) Liu, S.; Zhang, D.; Sheng, Y.; Zhang, W.; Qin, Z.; Qin, M.; Li, S.; Wang, Y.; Gao, C.; Wang, Q.; Ming, Y.; Liu, C.; Yang, K.; Huang, Q.; Qi, J.; Gao, Q.; Chen, K.; Hu, Y.; Rong, Y.; Lu, X.; Mei, A.; Han, H. Highly oriented $MAPbI_3$ crystals for efficient hole-conductor-free printable mesoscopic perovskite solar cells. *Fundam. Res.* **2022**, *2*, 276−283.

(3) Torabi, N.; Behjat, A.; Zhou, Y.; Docampo, P.; Stoddard, R. J.; Hillhouse, H. W.; Ameri, T. Progress and challenges in perovskite photovoltaics from single- to multi-junction cells. *Mater. Today Energy* **2019**, *12*, 70−94.

(4) Noh, J. H.; Im, S. H.; Heo, J. H.; Mandal, T. N.; Seok, S. I. Chemical management for colorful, efficient, and stable inorganic-organic hybrid nanostructured solar cells. *Nano Lett.* **2013**, *13*, 1764−1769.

(5) Zuo, C.; Bolink, H. J.; Han, H.; Huang, J.; Cahen, D.; Ding, L. Advances in Perovskite Solar Cells. *Adv. Sci.* **2016**, *3*, 1500324.

(6) Jung, E. H.; Jeon, N. J.; Park, E. Y.; Moon, C. S.; Shin, T. J.; Yang, T. Y.; Noh, J. H.; Seo, J. Efficient, stable and scalable perovskite solar cells using poly(3-hexylthiophene). *Nature* **2019**, *567*, 511−515.

(7) Jeon, N. J.; Noh, J. H.; Kim, Y. C.; Yang, W. S.; Ryu, S.; Seok, S. I. Solvent engineering for high-performance inorganic-organic hybrid perovskite solar cells. *Nat. Mater.* **2014**, *13*, 897−903.

(8) Wu, Y.; Xie, F.; Chen, H.; Yang, X.; Su, H.; Cai, M.; Zhou, Z.; Noda, T.; Han, L. Thermally stable $MAPbI_3$ perovskite solar cells with efficiency of 19.19% and area over 1 cm2 achieved by additive engineering. *Adv. Mater.* **2017**, *29*, 1701073.

(9) Chen, Z.; Turedi, B.; Alsalloum, A. Y.; Yang, C.; Zheng, X.; Gereige, I.; AlSaggaf, A.; Mohammed, O. F.; Bakr, O. M. Single-Crystal $MAPbI_3$ Perovskite Solar Cells Exceeding 21% Power Conversion Efficiency. *ACS Energy Lett.* **2019**, *4*, 1258−1259.

(10) Zhang, Y.; Chen, S.; Chen, H.; Zhang, G.; Zhao, M.; Zhao, C.; Guo, W.; Ji, W.; Shi, Z.; Jiu, T. Highly-improved performance of inverted planar perovskite solar cells by glucose modification. *J. Mater. Chem. C* **2020**, *8*, 5894−5903.

(11) Abdelmageed, G.; Jewell, L.; Hellier, K.; Seymour, L.; Luo, B.; Bridges, F.; Zhang, J. Z.; Carter, S. Mechanisms for light induced degradation in $MAPbI_3$ perovskite thin films and solar cells. *Appl. Phys. Lett.* **2016**, *109*, 233905.

(12) Frolova, L. A.; Dremova, N. N.; Troshin, P. A. The chemical origin of the p-type and n-type doping effects in the hybrid methylammonium-lead iodide (MAPbI3) perovskite solar cells. *Chem. Commun.* **2015**, *51*, 14917−14920.

(13) Han, Y.; Meyer, S.; Dkhissi, Y.; Weber, K.; Pringle, J. M.; Bach, U.; Spiccia, L.; Cheng, Y.-B. Degradation observations of encapsulated planar $CH_3NH_3PbI_3$ perovskite solar cells at high temperatures and humidity. *J. Mater. Chem. A* **2015**, *3*, 8139−8147.

(14) Cha, M.; Da, P.; Wang, J.; Wang, W.; Chen, Z.; Xiu, F.; Zheng, G.; Wang, Z. S. Enhancing Perovskite Solar Cell Performance by Interface Engineering Using CH3NH3PbBr0.9I2.1 Quantum Dots. *J. Am. Chem. Soc.* **2016**, *138*, 8581−8587.

(15) Ahn, N.; Son, D. Y.; Jang, I. H.; Kang, S. M.; Choi, M.; Park, N. G. Highly Reproducible Perovskite Solar Cells with Average Efficiency of 18.3% and Best Efficiency of 19.7% Fabricated via Lewis Base Adduct of Lead(II) Iodide. *J. Am. Chem. Soc.* **2015**, *137*, 8696−8699.

(16) Park, J. H.; Seo, J.; Park, S.; Shin, S. S.; Kim, Y. C.; Jeon, N. J.; Shin, H. W.; Ahn, T. K.; Noh, J. H.; Yoon, S. C.; Hwang, C. S.; Seok, S. I. Efficient CH3NH3PbI3Perovskite Solar Cells Employing Nanostructured p-Type NiO Electrode Formed by a Pulsed Laser Deposition. *Adv. Mater.* **2015**, *27*, 4013−4019.

(17) Kojima, A.; Teshima, K.; Shirai, Y.; Miyasaka, T. Organometal halide perovskites as visible-light sensitizers for photovoltaic cells. *J. Am. Chem. Soc.* **2009**, *131*, 6050−6051.

(18) National Renewable Energy Laboratory. Best Research Cell Efficiencies. 2022, https://www.nrel.gov/pv/cell-efficiency.html (accessed June 30, 2022).

(19) Said, A. A.; Xie, J.; Zhang, Q. Recent Progress in Organic Electron Transport Materials in Inverted Perovskite Solar Cells. *Small* **2019**, *15*, 1900854.

(20) Chen, J.; Park, N. G. Causes and Solutions of Recombination in Perovskite Solar Cells. *Adv. Mater.* **2019**, *31*, 1803019.

(21) Lee, D.-K.; Lim, K.-S.; Lee, J.-W.; Park, N.-G. Scalable perovskite coating via anti-solvent-free Lewis acid−base adduct engineering for efficient perovskite solar modules. *J. Mater. Chem. A* **2021**, *9*, 3018−3028.

(22) Manser, J. S.; Christians, J. A.; Kamat, P. V. Intriguing Optoelectronic Properties of Metal Halide Perovskites. *Chem. Rev.* **2016**, *116*, 12956−13008.

(23) Zhang, H.; Chen, H.; Stoumpos, C. C.; Ren, J.; Hou, Q.; Li, X.; Li, J.; He, H.; Lin, H.; Wang, J.; Hao, F.; Kanatzidis, M. G. Thiazole-Induced Surface Passivation and Recrystallization of $CH_3NH_3PbI_3$ Films for Perovskite Solar Cells with Ultrahigh Fill Factors. *ACS Appl. Mater. Interfaces* **2018**, *10*, 42436−42443.

(24) Liu, X.; Wu, J.; Guo, Q.; Yang, Y.; Luo, H.; Liu, Q.; Wang, X.; He, X.; Huang, M.; Lan, Z. Pyrrole: an additive for improving the

efficiency and stability of perovskite solar cells. *J. Mater. Chem. A* **2019**, *7*, 11764−11770.
(25) Deng, L.; Xie, S.; Gao, F. Fullerene-Based Materials for Photovoltaic Applications: Toward Efficient, Hysteresis-Free, and Stable Perovskite Solar Cells. Adv. *Electron. Mater.* **2018**, *4*, 1700435.
(26) Jia, L.; Chen, M.; Yang, S. Functionalization of fullerene materials toward applications in perovskite solar cells. *Mater. Chem. Front.* **2020**, *4*, 2256−2282.
(27) Noel, N. K.; Abate, A.; Stranks, S. D.; Parrott, E. S.; Burlakov, V. M.; Goriely, A.; Snaith, H. J. Enhanced photoluminescence and solar cell performance via Lewis base passivation of organic−inorganic lead halide perovskites. *ACS Nano* **2014**, *8*, 9815−9821.
(28) Lin, Y.; Shen, L.; Dai, J.; Deng, Y.; Wu, Y.; Bai, Y.; Zheng, X.; Wang, J.; Fang, Y.; Wei, H.; Ma, W.; Zeng, X. C.; Zhan, X.; Huang, J. π-conjugated Lewis Base: efficient trap-passivation and charge-extraction for hybrid perovskite solar cells. *Adv. Mater.* **2017**, *29*, 1604545.
(29) Zuo, L.; Guo, H.; deQuilettes, D. W.; Jariwala, S.; De Marco, N.; Dong, S.; DeBlock, R.; Ginger, D. S.; Dunn, B.; Wang, M.; Yang, Y. Polymer-modified halide perovskite films for efficient and stable planar heterojunction solar cells. *Sci. Adv.* **2017**, *3*, No. e1700106.
(30) Cao, J.; Yin, J.; Yuan, S.; Zhao, Y.; Li, J.; Zheng, N. Thiols as interfacial modifiers to enhance the performance and stability of perovskite solar cells. *Nanoscale* **2015**, *7*, 9443−9447.
(31) Wen, T. Y.; Yang, S.; Liu, P. F.; Tang, L. J.; Qiao, H. W.; Chen, X.; Yang, X. H.; Hou, Y.; Yang, H. G. Surface Electronic Modification of Perovskite Thin Film with Water-Resistant Electron Delocalized Molecules for Stable and Efficient Photovoltaics. *Adv. Energy Mater.* **2018**, *8*, 1703143.
(32) Zeng, Q.; Zhang, X.; Feng, X.; Lu, S.; Chen, Z.; Yong, X.; Redfern, S. A.; Wei, H.; Wang, H.; Shen, H.; Zhang, W.; Zheng, W.; Zhang, H.; Tse, J. S.; Yang, B. Polymer-passivated inorganic cesium lead mixed-halide perovskites for stable and efficient solar cells with high open-circuit voltage over 1.3 V. *Adv. Mater.* **2018**, *30*, 1705393.
(33) Eperon, G. E.; Habisreutinger, S. N.; Leijtens, T.; Bruijnaers, B. J.; van Franeker, J. J.; deQuilettes, D. W.; Pathak, S.; Sutton, R. J.; Grancini, G.; Ginger, D. S.; Janssen, R. A. J.; Petrozza, A.; Snaith, H. J. The importance of moisture in hybrid lead halide perovskite thin film fabrication. *ACS Nano* **2015**, *9*, 9380−9393.
(34) Li, W.; Dong, H.; Guo, X.; Li, N.; Li, J.; Niu, G.; Wang, L. Graphene oxide as dual functional interface modifier for improving wettability and retarding recombination in hybrid perovskite solar cells. *J. Mater. Chem. A* **2014**, *2*, 20105−20111.
(35) Palazon, F.; Pérez-del-Rey, D.; Marras, S.; Prato, M.; Sessolo, M.; Bolink, H. J.; Manna, L. Coating Evaporated MAPI Thin Films with Organic Molecules: Improved Stability at High Temperature and Implementation in High-Efficiency Solar Cells. *ACS Energy Lett.* **2018**, *3*, 835−839.
(36) deQuilettes, D. W.; Koch, S.; Burke, S.; Paranji, R. K.; Shropshire, A. J.; Ziffer, M. E.; Ginger, D. S. Photoluminescence lifetimes exceeding 8 μs and quantum yields exceeding 30% in hybrid perovskite thin films by ligand passivation. *ACS Energy Lett.* **2016**, *1*, 438−444.
(37) Braly, I. L.; deQuilettes, D. W.; Pazos-Outón, L. M.; Burke, S.; Ziffer, M. E.; Ginger, D. S.; Hillhouse, H. W. Hybrid perovskite films approaching the radiative limit with over 90% photoluminescence quantum efficiency. *Nat. Photonics* **2018**, *12*, 355−361.
(38) Zhu, J.; Kim, D. H.; Kim, J. D.; Lee, D. G.; Kim, W. B.; Chen, S. w.; Kim, J. Y.; Lee, J. M.; Lee, H.; Han, G. S.; Ahn, T. K.; Jung, H. S. All-in-One Lewis Base for Enhanced Precursor and Device Stability in Highly Efficient Perovskite Solar Cells. *ACS Energy Lett.* **2021**, *6*, 3425−3434.
(39) Wang, S.; Yang, B.; Han, J.; He, Z.; Li, T.; Cao, Q.; Yang, J.; Suo, J.; Li, X.; Liu, Z.; Liu, S.; Tang, C.; Hagfeldt, A. Polymeric room-temperature molten salt as a multifunctional additive toward highly efficient and stable inverted planar perovskite solar cells. *Energy Environ. Sci.* **2020**, *13*, 5068−5079.
(40) Koo, D.; Cho, Y.; Kim, U.; Jeong, G.; Lee, J.; Seo, J.; Yang, C.; Park, H. High-performance inverted perovskite solar cells with operational stability via n-type small molecule additive-assisted defect passivation. *Adv. Energy Mater.* **2020**, *10*, 2001920.
(41) Song, S.; Park, E. Y.; Ma, B. S.; Kim, D. J.; Park, H. H.; Kim, Y. Y.; Shin, S. S.; Jeon, N. J.; Kim, T. S.; Seo, J. Selective defect passivation and topographical control of 4-dimethylaminopyridine at grain boundary for efficient and stable planar perovskite solar cells. *Adv. Energy Mater.* **2021**, *11*, 2003382.
(42) Han, W.; Liu, X.; Zhang, X.; Ding, Y.; Guo, Y. Bifunctional-based small molecule as multifunctional additive for improved performance of perovskite solar cells. *Org. Electron.* **2021**, *96*, 106226.
(43) Ram, V. J.; Sethi, A.; Nath, M.; Pratap, R. Five-Membered Heterocycles. *The Chemistry of Heterocycles*; Elsevier, 2019; pp 149−478.
(44) Pairas, G. N.; Perperopoulou, F.; Tsoungas, P. G.; Varvounis, G. The Isoxazole Ring and Its N-Oxide: A Privileged Core Structure in Neuropsychiatric Therapeutics. *ChemMedChem* **2017**, *12*, 408−419.
(45) Zhu, J.; Mo, J.; Lin, H. Z.; Chen, Y.; Sun, H. P. The recent progress of isoxazole in medicinal chemistry. *Bioorg. Med. Chem.* **2018**, *26*, 3065−3075.
(46) Sherkar, T. S.; Momblona, C.; Gil-Escrig, L.; Ávila, J.; Sessolo, M.; Bolink, H. J.; Koster, L. J. A. Recombination in Perovskite Solar Cells: Significance of Grain Boundaries, Interface Traps, and Defect Ions. *ACS Energy Lett.* **2017**, *2*, 1214−1222.
(47) Jacobsson, T. J.; Correa-Baena, J. P.; Halvani Anaraki, E.; Philippe, B.; Stranks, S. D.; Bouduban, M. E.; Tress, W.; Schenk, K.; Teuscher, J.; Moser, J. E.; Rensmo, H.; Hagfeldt, A. Unreacted PbI_2 as a Double-Edged Sword for Enhancing the Performance of Perovskite Solar Cells. *J. Am. Chem. Soc.* **2016**, *138*, 10331−10343.
(48) Chen, B.; Rudd, P. N.; Yang, S.; Yuan, Y.; Huang, J. Imperfections and their passivation in halide perovskite solar cells. *Chem. Soc. Rev.* **2019**, *48*, 3842−3867.
(49) Xie, H.; Liu, X.; Lyu, L.; Niu, D.; Wang, Q.; Huang, J.; Gao, Y. Effects of Precursor Ratios and Annealing on Electronic Structure and Surface Composition of $CH_3NH_3PbI_3$ Perovskite Films. *J. Phys. Chem. C* **2015**, *120*, 215−220.
(50) Xu, H.; Wu, Y.; Cui, J.; Ni, C.; Xu, F.; Cai, J.; Hong, F.; Fang, Z.; Wang, W.; Zhu, J.; Wang, L.; Xu, R.; Xu, F. Formation and evolution of the unexpected PbI_2 phase at the interface during the growth of evaporated perovskite films. *Phys. Chem. Chem. Phys.* **2016**, *18*, 18607−18613.
(51) Wang, R.; Xue, J.; Wang, K.-L.; Wang, Z.-K.; Luo, Y.; Fenning, D.; Xu, G.; Nuryyeva, S.; Huang, T.; Zhao, Y.; Yang, J. L.; Zhu, J.; Wang, M.; Tan, S.; Yavuz, I.; Houk, K. N.; Yang, Y. Constructive molecular configurations for surface-defect passivation of perovskite photovoltaics. *Science* **2019**, *366*, 1509−1513.
(52) Ak, M.; Gacal, B.; Kiskan, B.; Yagci, Y.; Toppare, L. Enhancing electrochromic properties of polypyrrole by silsesquioxane nanocages. *Polymer* **2008**, *49*, 2202−2210.
(53) Fu, J.; Liu, W.; Hao, Z.; Wu, J.; Yin, A.; Panjiyar, X.; Liu, J.; Shen, H.; Wang, H. Characterization of a low shrinkage dental composite containing bismethylene spiroorthocarbonate expanding monomer. *Int. J. Mol. Sci.* **2014**, *15*, 2400−2412.
(54) Bi, D.; Yi, C.; Luo, J.; Décoppet, J. D.; Zhang, F.; Zakeeruddin, S. M.; Li, X.; Hagfeldt, A.; Grätzel, M. Polymer-templated nucleation and crystal growth of perovskite films for solar cells with efficiency greater than 21. *Nat. Energy* **2016**, *1*, 16142.
(55) Leguy, A. M.; Azarhoosh, P.; Alonso, M. I.; Campoy-Quiles, M.; Weber, O. J.; Yao, J.; Bryant, D.; Weller, M. T.; Nelson, J.; Walsh, A.; van Schilfgaarde, M.; Barnes, P. R. Experimental and theoretical optical properties of methylammonium lead halide perovskites. *Nanoscale* **2016**, *8*, 6317−6327.
(56) Wen, X.; Wu, J.; Gao, D.; Lin, C. Interfacial engineering with amino-functionalized graphene for efficient perovskite solar cells. *J. Mater. Chem. A* **2016**, *4*, 13482−13487.
(57) Li, G.; Wu, J.; Song, J.; Meng, C.; Song, Z.; Wang, X.; Liu, X.; Yang, Y.; Wang, D.; Lan, Z. Excellent quinoline additive in perovskite toward to efficient and stable perovskite solar cells. *J. Power Sources* **2021**, *481*, 228857.

https://doi.org/10.1021/acsomega.2c03775
ACS Omega 2022, 7, 34278−34285

(58) Mohanta, D.; Narayanan, S. S.; Pal, S. K.; Raychaudhuri, A. K. Time-resolved photoluminescence decay characteristics of bovine serum albumin-conjugated semiconductor nanocrystallites. *J. Exp. Nanosci.* **2009**, *4*, 177−191.
(59) Chen, C. I.; Wu, S.; Lu, Y. A.; Lee, C. C.; Ho, K. C.; Zhu, Z.; Chen, W. C.; Chueh, C. C. Enhanced Near-Infrared Photoresponse of Inverted Perovskite Solar Cells Through Rational Design of Bulk-Heterojunction Electron-Transporting Layers. *Adv. Sci.* **2019**, *6*, 1901714.
(60) Zhao, Q.; Wu, R.; Zhang, Z.; Xiong, J.; He, Z.; Fan, B.; Dai, Z.; Yang, B.; Xue, X.; Cai, P.; Zhan, S.; Zhang, X.; Zhang, J. Achieving efficient inverted planar perovskite solar cells with nondoped PTAA as a hole transport layer. *Org. Electron.* **2019**, *71*, 106−112.
(61) Luo, D.; Su, R.; Zhang, W.; Gong, Q.; Zhu, R. Minimizing non-radiative recombination losses in perovskite solar cells. *Nat. Rev. Mater.* **2019**, *5*, 44−60.
(62) Habisreutinger, S. N.; Noel, N. K.; Snaith, H. J. Hysteresis Index: A Figure without Merit for Quantifying Hysteresis in Perovskite Solar Cells. *ACS Energy Lett.* **2018**, *3*, 2472−2476.
(63) Hanmandlu, C.; Swamy, S.; Singh, A.; Hsin-An Chen, C.; Liu, C.-C.; Lai, C.-S.; Mohapatra, A.; Pao, C.-W.; Chen, P.; Chu, C.-W. Suppression of surface defects to achieve hysteresis-free inverted perovskite solar cells via quantum dot passivation. *J. Mater. Chem. A* **2020**, *8*, 5263−5274.
(64) Miller, D. W.; Eperon, G. E.; Roe, E. T.; Warren, C. W.; Snaith, H. J.; Lonergan, M. C. Defect states in perovskite solar cells associated with hysteresis and performance. *Appl. Phys. Lett.* **2016**, *109*, 153902.
(65) Tao, L.; Huo, Z.; Ding, Y.; Li, Y.; Dai, S.; Wang, L.; Zhu, J.; Pan, X.; Zhang, B.; Yao, J.; Nazeeruddin, M. K.; Grätzel, M. High-efficiency and stable quasi-solid-state dye-sensitized solar cell based on low molecular mass organogelator electrolyte. *J. Mater. Chem. A* **2015**, *3*, 2344−2352.
(66) Jiang, J.; Wang, Q.; Jin, Z.; Zhang, X.; Lei, J.; Bin, H.; Zhang, Z. G.; Li, Y.; Liu, S. Polymer doping for high-efficiency perovskite solar cells with improved moisture stability. *Adv. Energy Mater.* **2018**, *8*, 1701757.
(67) Duan, J.; Zhao, Y.; He, B.; Tang, Q. High-Purity Inorganic Perovskite Films for Solar Cells with 9.72 % Efficiency. *Angew. Chem., Int. Ed.* **2018**, *57*, 3787−3791.
(68) Li, H.; Tong, G.; Chen, T.; Zhu, H.; Li, G.; Chang, Y.; Wang, L.; Jiang, Y. Interface engineering using a perovskite derivative phase for efficient and stable $CsPbBr_3$ solar cells. *J. Mater. Chem. A* **2018**, *6*, 14255−14261.
(69) Yin, P.; Zheng, T.; Wu, Y.; Liu, G.; Zhang, Z.-G.; Cui, C.; Li, Y.; Shen, P. Achieving efficient thick active layer and large area ternary polymer solar cells by incorporating a new fused heptacyclic non-fullerene acceptor. *J. Mater. Chem. A* **2018**, *6*, 20313−20326.
(70) Lampert, M. A.; Mark, P. *Current Injection in Solids*; Academic press, 1970.
(71) Anusca, I.; Balčiūnas, S.; Gemeiner, P.; Svirskas, Š.; Sanlialp, M.; Lackner, G.; Fettkenhauer, C.; Belovickis, J.; Samulionis, V.; Ivanov, M.; Dkhil, B.; Banys, J.; Shvartsman, V. V.; Lupascu, D. C. Dielectric response: answer to many questions in the methylammonium lead halide solar cell absorbers. *Adv. Energy Mater.* **2017**, *7*, 1700600.
(72) Senocrate, A.; Acartürk, T.; Kim, G. Y.; Merkle, R.; Starke, U.; Grätzel, M.; Maier, J. Interaction of oxygen with halide perovskites. *J. Mater. Chem. A* **2018**, *6*, 10847−10855.
(73) Huang, J.; Tan, S.; Lund, P. D.; Zhou, H. Impact of H_2O on organic−inorganic hybrid perovskite solar cells. *Energy Environ. Sci.* **2017**, *10*, 2284−2311.
(74) Cao, J.; Loi, H. L.; Xu, Y.; Guo, X.; Wang, N.; Liu, C. K.; Wang, T.; Cheng, H.; Zhu, Y.; Li, M. G.; Wong, W. Y.; Yan, F. High-Performance Tin-Lead Mixed-Perovskite Solar Cells with Vertical Compositioal Gradient. *Adv. Mater.* **2022**, *34*, 2107729.
(75) Deng, X.; Wen, X.; Zheng, J.; Young, T.; Lau, C. F. J.; Kim, J.; Green, M.; Huang, S.; Ho-Baillie, A. Dynamic study of the light soaking effect on perovskite solar cells by in-situ photoluminescence microscopy. *Nano Energy* **2018**, *46*, 356−364.

https://doi.org/10.1021/acsomega.2c03775
ACS Omega 2022, 7, 34278−34285